






## Multi-omics delineation of cytokine-induced endothelial inflammatory states

Stijn A. Groten<sup>1</sup>, Eva R. Smit<sup>1</sup>, Esmée F. J. Janssen<sup>1</sup>, Bart L. van den Eshof <sup>1</sup>, Floris P. J. van Alphen<sup>1</sup>, Carmen van der Zwaan<sup>1</sup>, Alexander B. Meijer<sup>1,2</sup>, Arie J. Hoogendijk <sup>1,3</sup> & Maartje van den Biggelaar <sup>1,3</sup> 

Vascular endothelial cells (ECs) form a dynamic interface between blood and tissue and play a crucial role in the progression of vascular inflammation. Here, we aim to dissect the system-wide molecular mechanisms of inflammatory endothelial-cytokine responses. Applying an unbiased cytokine library, we determined that TNF $\alpha$  and IFN $\gamma$  induced the largest EC response resulting in distinct proteomic inflammatory signatures. Notably, combined TNF $\alpha$  + IFN $\gamma$  stimulation induced an additional synergetic inflammatory signature. We employed a multi-omics approach to dissect these inflammatory states, combining (phospho-) proteome, transcriptome and secretome and found, depending on the stimulus, a wide-array of altered immune-modulating processes, including complement proteins, MHC complexes and distinct secretory cytokines. Synergy resulted in cooperative activation of transcript induction. This resource describes the intricate molecular mechanisms that are at the basis of endothelial inflammation and supports the adaptive immunomodulatory role of the endothelium in host defense and vascular inflammation.

<sup>1</sup>Department of Molecular Hematology, Sanquin Research, Amsterdam 1066 CX, The Netherlands. <sup>2</sup>Department of Biomolecular Mass Spectrometry and Proteomics, Utrecht Institute for Pharmaceutical Sciences (UIPS), Utrecht University, Utrecht 3584 CS, The Netherlands. <sup>3</sup>These authors contributed equally: Arie J. Hoogendijk, Maartje van den Biggelaar. email: [m.vandenbiggelaar@sanquin.nl](mailto:m.vandenbiggelaar@sanquin.nl)

Endothelial cells (ECs) line the inside of our blood vessels and form a dynamic interface between blood and surrounding tissues. Apart from facilitating oxygen, nutrient, and waste product exchange, ECs control hemostasis by attracting platelets to seal breaches in the vascular walls during primary hemostasis<sup>1</sup>. Moreover, ECs are crucial gatekeepers controlling the trafficking of immune cells into and out of tissues during inflammation. For their role in this adaptive synapse, ECs are well-equipped to sense environmental cues, such as mechanical stress, hormones (e.g., vasopressin, histamine), cells (e.g., neutrophils, monocytes, platelets) and other external stimuli (e.g., thrombin, cytokines)<sup>2–5</sup>. In addition to the transmigration of immune cells, ECs have several immunomodulatory capacities such as antigen presentation and cytokine secretion<sup>5,6</sup>. However, although ECs carry these immune-modulating properties and are among the first cells to come into contact with pathogens, they are rarely mentioned in immune cell networks<sup>7–9</sup>.

Deregulation of EC homeostasis can result in over-inflammatory or hyper-coagulation states of the endothelium. This endothelial dysfunction is implicated in several multifaceted inflammatory diseases, including transfusion related acute lung injury, sepsis, rheumatoid arthritis, acute respiratory distress syndrome (ARDS), eye vasculopathies, chronic kidney disease and COVID-19<sup>10–19</sup>.

Although both endothelial homeostasis and cytokines are deregulated in these diseases, the molecular basis which orchestrates adaptive endothelial-cytokine interactions is mostly confined to research on tumor necrosis factor-alpha (TNF $\alpha$ ). Moreover, synergism between cytokines such as TNF $\alpha$  and interferon-gamma (IFN $\gamma$ ) has been observed in ECs and linked to detrimental effects in inflammatory disorders<sup>20–23</sup>. Although underlying mechanisms have been proposed, a system-wide EC response has not been characterized.

Therefore, in this study, we set out to dissect the molecular signatures of endothelial-cytokine responses, employing blood outgrowth endothelial cells (BOECs), also known as endothelial colony forming cells, as our source of ECs because of their extensive, robust expansion, expression of mature vascular EC markers and ability to be isolated from adult donors<sup>24,25</sup>.

We show that ECs express the receptor-repertoire to facilitate various cytokine signals. However, upon stimulation with an unbiased cytokine library, we observed predominantly unique inflammatory states for TNF $\alpha$  and IFN $\gamma$ . Moreover, combined stimulation of TNF $\alpha$  and IFN $\gamma$  resulted in a synergetic EC response. Combining multiple omics levels, we dissected the

molecular basis of these inflammatory states from signaling (phosphoproteome) to mRNA transcription (transcriptome), protein regulation (proteome) and protein secretion (secretome). This study reveals system-wide adaptive EC inflammatory states, emphasizing the role of EC-cytokine interactions in inflammatory pathogenesis and reiterating ECs as an adaptive player in inflammation.

## Results

**Mapping cytokine-endothelial interactions.** Although vascular inflammation is orchestrated by cytokines that activate the endothelium, knowledge on endothelial-cytokine interactions at the system level is limited. To review established interactions, we used immuneXpresso, a text mining engine that extracts directional cell-cytokine interactions from PubMed abstracts<sup>26</sup>. Of the 143 cytokines present in this database, 65 were identified to interact with ECs. Most studies report the interaction with cytokine TNF $\alpha$  and fibroblast growth factor 2 (FGF2) (Fig. 1a). To determine whether this is due to a confirmation bias in literature or whether ECs do not express the receptors to interact with other cytokines, we performed an in-depth proteomic analysis of BOECs to determine the receptor-repertoire. Out of 6848 quantified proteins, we found 166 receptors with known ligand interactions<sup>8</sup> (Fig. 1b and Supplementary Fig. 1a), showing that ECs possess a wide array of receptors that can interact with ligands present in their microenvironment.

**Proteome response profiling of EC-cytokine interactions.** Next, we profiled EC responses to different cytokines and stimulated BOECs with a library of 92 signaling proteins based on commercial availability. This library contained 46 proteins from the ImmuneXpresso search including both TNF $\alpha$  and FGF2 (Supplementary Table 1). BOECs were stimulated for 24 h and proteomics responses were analyzed using high-resolution label-free quantitative (LFQ) MS. We quantified a total of 4790 proteins with an overall median Pearson correlation coefficient of 0.96 (Supplementary Fig. 2). Of the 92 signaling proteins, 47 had an impact on the proteome and in total 293 proteins were differentially abundant (Fig. 2a). TNF $\alpha$  stimulation induced the strongest response, followed by IFN $\gamma$ , IL1 $\beta$  and IL1 $\alpha$ . To visualize response similarities between stimuli, we constructed a network of the number of differentially abundant proteins and overlap per stimulus (Fig. 2b and Supplementary Fig. 3a). This revealed TNF $\alpha$  as a central “knot” overlapping with 7 other cytokines. The highest similarity was observed between TNF $\alpha$ , IL1 $\alpha$  and IL1 $\beta$ . We also observed an

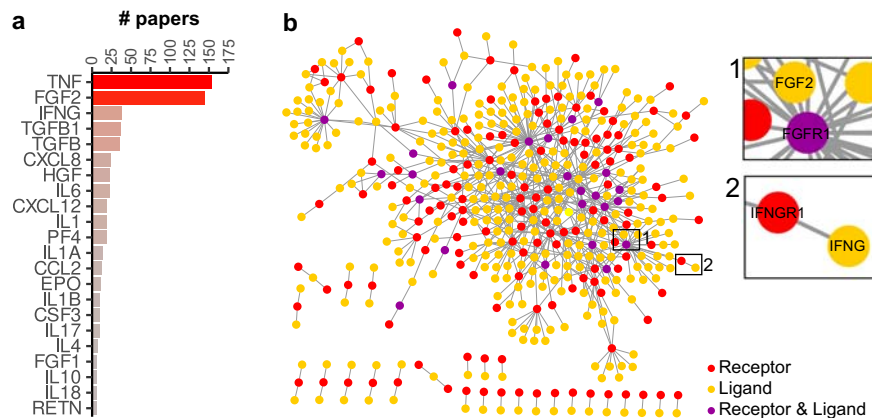


**Fig. 1** Knowledge-based mapping of cytokine-endothelial interactions. **a** Bar plot based on immuneXpresso data mining showing the number of papers describing interactions between the cytokines and endothelial cells (# papers > 5). **b** Cytoscape interaction network of receptors and potential ligands (red dots: receptors, yellow dots: ligands, purple dots: proteins fulfilling both receptor and ligand criteria), edges represent STRING-DB scores. Inserts show zooms of example cytokine-receptor interactions; for network with labels, see Supplementary Fig. 1b.

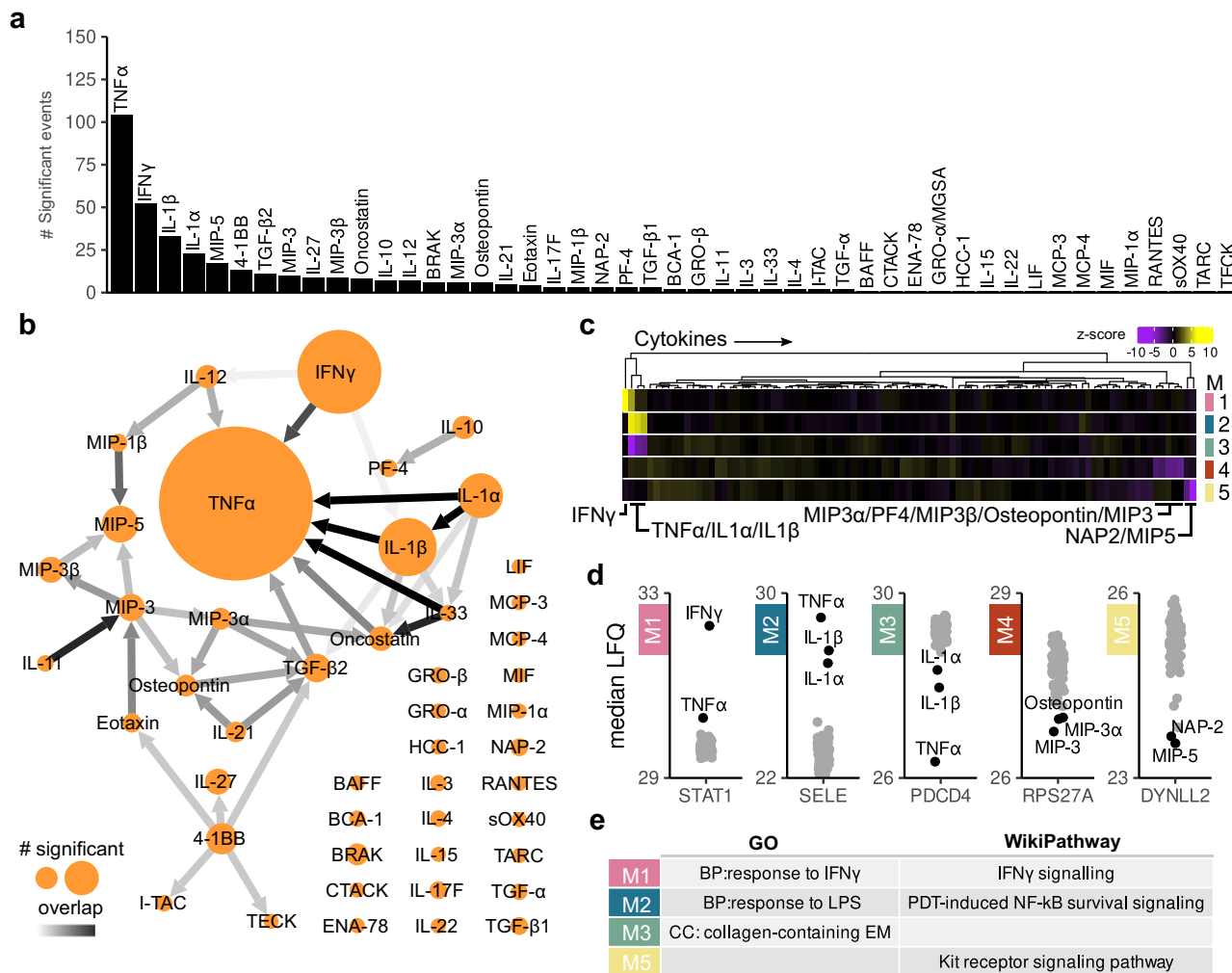


**Fig. 2 Proteome response profiling of EC-cytokine interactions.** **a** Bar plot showing the amount of differentially regulated proteins for the stimuli that altered the BOEC proteome after 24 h of stimulation (moderated *t*-test, Benjamini-Hochberg (BH) adjusted *p* value < 0.05 and log2 fold change > 1). **b** Summarizing network of differentially abundant proteins between stimuli. Node labels show cytokine stimuli. Node size represents amount of statistically significant proteins. Edges show overlap between proteomes, color intensities (white to black) of edges indicate amount of overlapping proteins as a ratio of the smaller node. See Supplementary Fig. 3 for non-summarized network. **c** Profile plots of modules describing cytokine proteomic responses with cytokine annotation. Gradient scale indicated z-scores of median LFQ-score of genes in a module per stimulus, Yellow: cytokines related to an increased abundance response profile; purple: cytokine(s) related to a decreased protein abundance response, cytokines which contribute to the module regulation are highlighted. Replicates have been summarized to medians for visualization, modules are indicated by color, M1 (pink), M2 (blue), M3 (green), M4 (red) and M5 (yellow). **d** Proteins with high modules membership scores plotted as median label-free intensities (LFQ). **e** Enriched GO terms and WikiPathways per module. MF molecular function, CC cellular component, BP biological process.

overlap between IL-33-TNF $\alpha$ , IL-33-Oncostatin and IL-11-MIP3. Co-expression-based clustering delineated 5 dominant EC response types (Fig. 2c). These consisted of two modules with increased proteins abundances (Modules 1 and 2: IFN $\gamma$  and TNF $\alpha$ /IL1 $\alpha$ /IL1 $\beta$  responses) and three reduced protein abundance modules (Modules 3-5, representing TNF $\alpha$ /IL1 $\alpha$ /IL1 $\beta$ , MIP5/NAP2 and MIP3/MIP3B/MIP3A/Osteopontin/PF4). Proteins with high module memberships, highlighted hallmark IFN $\gamma$  and TNF $\alpha$  responsive proteins Signal transducer and activator of transcription 1-alpha/beta (*STAT1*) and E-selectin (*SELE*) for modules 1 and 2 (Fig. 2d). Gene Ontology (GO) enrichment and pathway analysis<sup>27</sup> revealed that module 1 enriched for “response to IFN $\gamma$ ” and “IFN $\gamma$  signaling” as expected, while module 2 consisted of “response to LPS” and NF- $\kappa$ B signaling. Module 3 enriched for extracellular component “collagen-containing extracellular matrix” and module 5 for “Kit receptor signaling pathway”. There was no significant enrichment for module 4 (Fig. 2e and Supplementary Fig. 3b, c).

**Combined TNF $\alpha$  and IFN $\gamma$  stimulation induces synergetic EC effects.** As TNF $\alpha$  and IFN $\gamma$  induced the highest, predominantly upregulated, responses and synergism between TNF $\alpha$  and IFN $\gamma$  has been reported, we assessed the effects of combining both cytokines. Initially, we studied EC morphology, and as expected, TNF $\alpha$ -stimulated cells shifted from a cobblestone round-like morphology to an elongated shape (Fig. 3a). Although IFN $\gamma$  did not induce observable changes, the combination of both stimuli resulted in an amplified TNF $\alpha$  morphology, in which all ECs changed to an elongated shape and a more contracted monolayer. Guided by these observations, we tested whether the proteome was impacted similarly using LFQ MS. Initially, we performed a concentration range of TNF $\alpha$  and IFN $\gamma$  separately and observed similar proteomic profiles for stimulation at 10 and 100 ng/ml (Supplementary Fig. 4). Stimulation with TNF $\alpha$ , IFN $\gamma$  and in combination resulted in three distinct signatures (Fig. 3b). Compared between each other, TNF $\alpha$  and IFN $\gamma$  induced 74

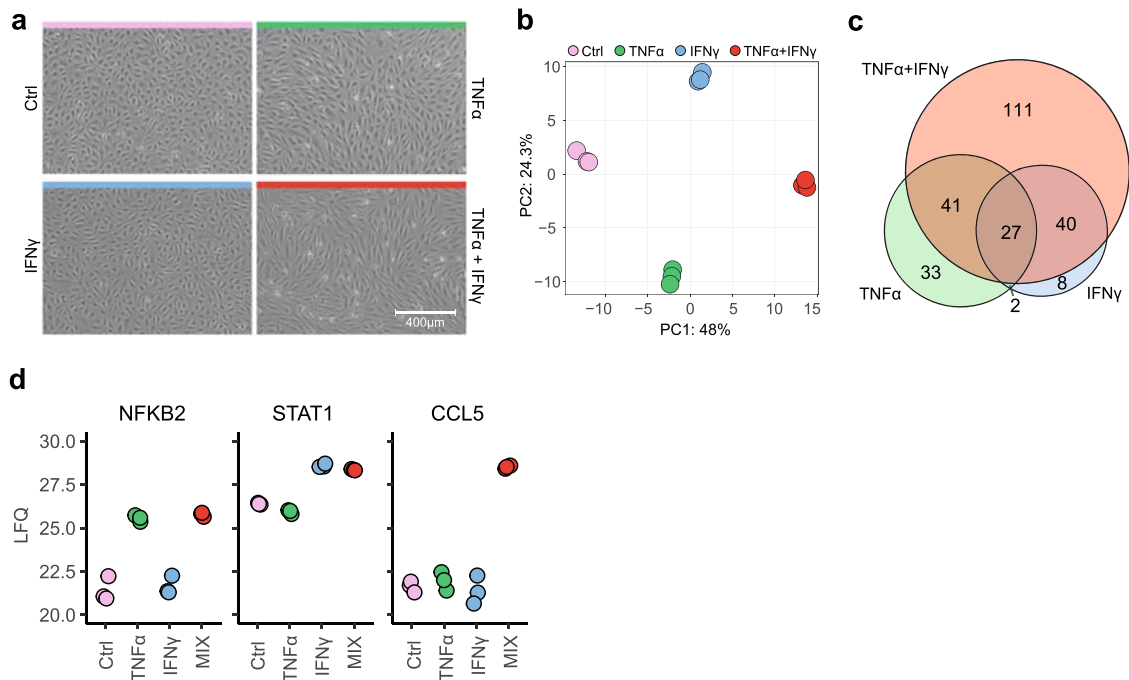


**Fig. 3 Synergistic proteomics response of TNF $\alpha$  and IFN $\gamma$  in ECs.** **a** Brightfield images of unstimulated ECs (Ctrl, pink) or ECs stimulated with TNF $\alpha$  (green), IFN $\gamma$  (blue) or TNF $\alpha$  + IFN $\gamma$  (red) for 24 h. **b** Principal component analysis (PCA) of proteomes of ECs stimulated with TNF $\alpha$ , IFN $\gamma$  and TNF $\alpha$  + IFN $\gamma$ . **c** Euler plot of total amount of unique and overlapping differentially regulated proteins per stimulus (moderated *t*-test, BH-adjusted  $p < 0.05$  and log<sub>2</sub> fold change > 1). **d** Lfq intensities of hallmark proteins per stimulation.

versus 48 unique proteins, respectively, while combined stimulation induced 111 unique altered protein abundances (Fig. 3c). Unique proteins per stimulus included transcription factors *NFKB2* and *STAT1* for TNF $\alpha$  and IFN $\gamma$  respectively and chemokine *CCL5* for combined stimulation (Fig. 3d).

### Temporal dynamics of TNF $\alpha$ and IFN $\gamma$ stimulation on phosphoproteome, transcriptome and proteome reveal systemwide inflammation states.

Prompted by the distinct proteomic signatures of TNF $\alpha$ , IFN $\gamma$  and combined stimulation and the notion that these cytokines are an object of extensive study in ECs, we aimed to dissect the molecular basis of the observed inflammatory states. To this end we employed several omics levels (phosphoproteome, transcriptome and proteome) in a time-resolved experiment to delineate the cytokine responses (Fig. 4a). To accurately quantify phosphopeptide levels we utilized a SILAC-MS workflow. Phosphoproteomes and proteomes were acquired from the same sample, whereas transcriptomic data were obtained from parallel stimulations. We quantified 4171 proteins, 6144 phosphosites and 60,664 transcripts. On all levels, TNF $\alpha$  + IFN $\gamma$  stimulation increased the number of significant events, compared to single stimuli (Fig. 4b). Transcript levels had the largest increase in events after combined stimulation compared to single stimuli (3.7-fold), while proteomic events increased less (2.3-fold). To visualize the regulatory dynamics between different omics levels, we evaluated the timing of these events. In line with the type 1–2 EC activation paradigm<sup>28</sup>, phosphoregulation occurred first (0–30 m), followed by transcriptomic (4–12 h) and proteomic events (8–24 h) (Fig. 4c). Furthermore, this analysis showed different dynamics between stimuli. The number of TNF $\alpha$ -induced transcriptomic events decreased after 12 h, while for IFN $\gamma$ , this number remained stable. Next, we performed GO-term enrichment analyses and compared enriched terms between omics levels and stimulations. Early responses, characterized by changes in phosphosites, reflected

mostly mechanical changes (e.g., cadherin binding and focal adhesion) and were shared between all stimulations (Fig. 4d). Enrichment of differentially regulated mRNAs included GO-terms “ECM organization” and “growth factor binding”, while proteome enriched for antigen presentation processes such as “MHC protein complex”, “peptide antigen binding” and the generic term “response to IFN $\gamma$ ”. To show the temporal nature of the omics levels, we plotted examples of each: phosphosite *ARHGEF10* S379, and the transcript and protein levels of *ICAM1* (Fig. 4e). The *ARHGEF10* phosphosite was dephosphorylated within 2 min, while mRNA levels of *ICAM1* peaked from 30 min to 4 h and approached baseline after 24 h. This pattern was followed by a steady increase in protein level reaching its peak at 24 h. To assess how the steady-state repertoire of BOECs compared to other EC types, we compared our RNAseq data to three published studies on various cultured primary ECs within the endoDB<sup>29–35</sup>. Principal component analysis showed high overlap with HUVECs in Rombouts et al.<sup>32,34</sup> and BOECs and pulmonary ECs in Long et al.<sup>31,35</sup> (Supplementary Fig. 5a). However, the correlation of transcriptome signatures also highlighted study-induced variation (Supplementary Fig. 5b). Relative expression levels of key EC genes as well as TNF $\alpha$  and IFN $\gamma$  receptors were similar between the majority of EC types (Supplementary Fig. 5c).

### Visualizing endothelial inflammatory states.

To visualize the processes that are driven by either TNF $\alpha$ , IFN $\gamma$  or combined stimulation, we generated a map of EC responses. First, we classified all differentially regulated phosphosites, transcripts and proteins as “TNF $\alpha$ ”, “IFN $\gamma$ ”, “common”, “TNF $\alpha$  + IFN $\gamma$ ” or “not classified”, based on effect sizes and dynamic behavior in time (Fig. 5a). For phosphosites most hits were classified as “common”, while for both mRNA and protein “IFN $\gamma$ ” was the most prevalent classifier (1850 transcripts and 60 proteins), followed by “TNF $\alpha$  + IFN $\gamma$ ” (1235 and 45) and “TNF $\alpha$ ” (948 and 34) (Fig. 5b). As an example of each classification, we plotted highly

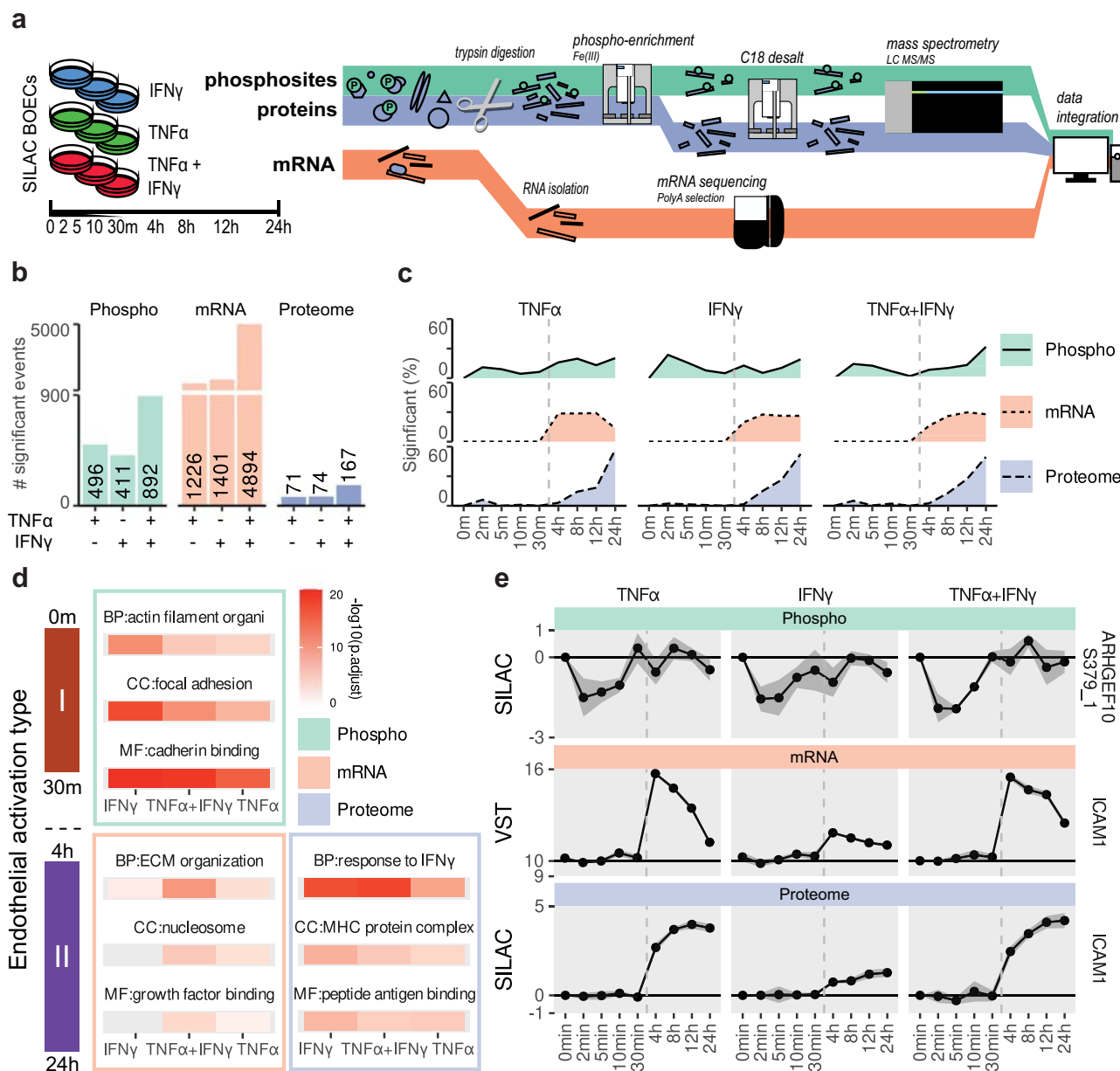


**Fig. 4** Temporal multi-omics analysis of TNF $\alpha$ , IFN $\gamma$  and combined stimulation responses. **a** Schematic overview of cell stimulation and multi-omic workflow. **b** Bar plot of total statistically significant events per stimulus on phosphoproteome (teal), transcriptome (orange) and proteome (purple) levels (moderated  $t$ -test, BH-adjusted  $p < 0.05$  and  $\log_2$  fold change  $> 1$ ). **c** Area plots of cumulative temporal dynamics of changes in the phosphoproteome (teal areas and solid lines), transcriptome (brown area and dotted lines) and proteome (purple areas and dashed lines). **d** Tile plot of the top enriched GO terms per stimulation: IFN $\gamma$  (pink), TNF $\alpha$  (orange), TNF $\alpha$  + IFN $\gamma$  (green) and omics level (as indicated). Color gradient indicated  $-\log_{10}$  BH-adjusted  $p$  values. MF: molecular function, CC: cellular component, BP: biological process. **e** Line plots of phosphorylation events, transcript levels and relative protein abundances of members of highly enriched GO-terms. Circles indicate medians; error bars show standard deviations ( $n = 3$  biological replicates).

correlating transcripts *NFKBIE* (“TNF $\alpha$ ”), *SECTM1* (“IFN $\gamma$ ”), *PARP10* (“common”) and *CCL8* (“TNF $\alpha$  + IFN $\gamma$ ”) (Fig. 5c). Next, we connected regulated features by querying the STRING database for high confidence ( $>0.95$ ) interactions. This resulted in a network containing 2306 interactions, revealing 9 high-density hubs summarized in biological processes: “Viral sensors”, “Cytokines”, “Complement factors”, “JAK/STAT signaling”, “Cell cycle”, “NFKB signaling”, “Proteasome”, “NFKB complex” and “Antigen presentation” (Fig. 5d and Supplementary Fig. 6). Plotting the ratio of response classifications per hub, only two were majorly TNF $\alpha$  induced: NF- $\kappa$ B complex proteins (47% TNF $\alpha$ ) and cytokines (44% TNF $\alpha$ ), while all others were primarily IFN $\gamma$ -induced. Especially the hubs, “Complement factors”, “Viral sensors”,

“Proteasome” and “Antigen presentation” were predominantly IFN $\gamma$ -induced ( $>75\%$ ). None of the hubs were majorly synergistically induced, suggesting synergy is confined to specific proteins and not entire biological processes.

**IFN $\gamma$ -induced immune repertoire of ECs.** To delineate biological processes from this multi-omics integration, we dissected the IFN $\gamma$  induced processes, as these covered mostly immune mediating processes. The “viral sensors” hub contains innate antiviral proteins *IFIT2*, *IFIT3*, *IFIH1*, *DDX58* and *GPB1* and *GPB2* which were all induced by IFN $\gamma$  (Fig. 6a). Interestingly, although protein changes generally occur at later timepoints and induced lower log-fold changes than mRNA, *DDX58* is an

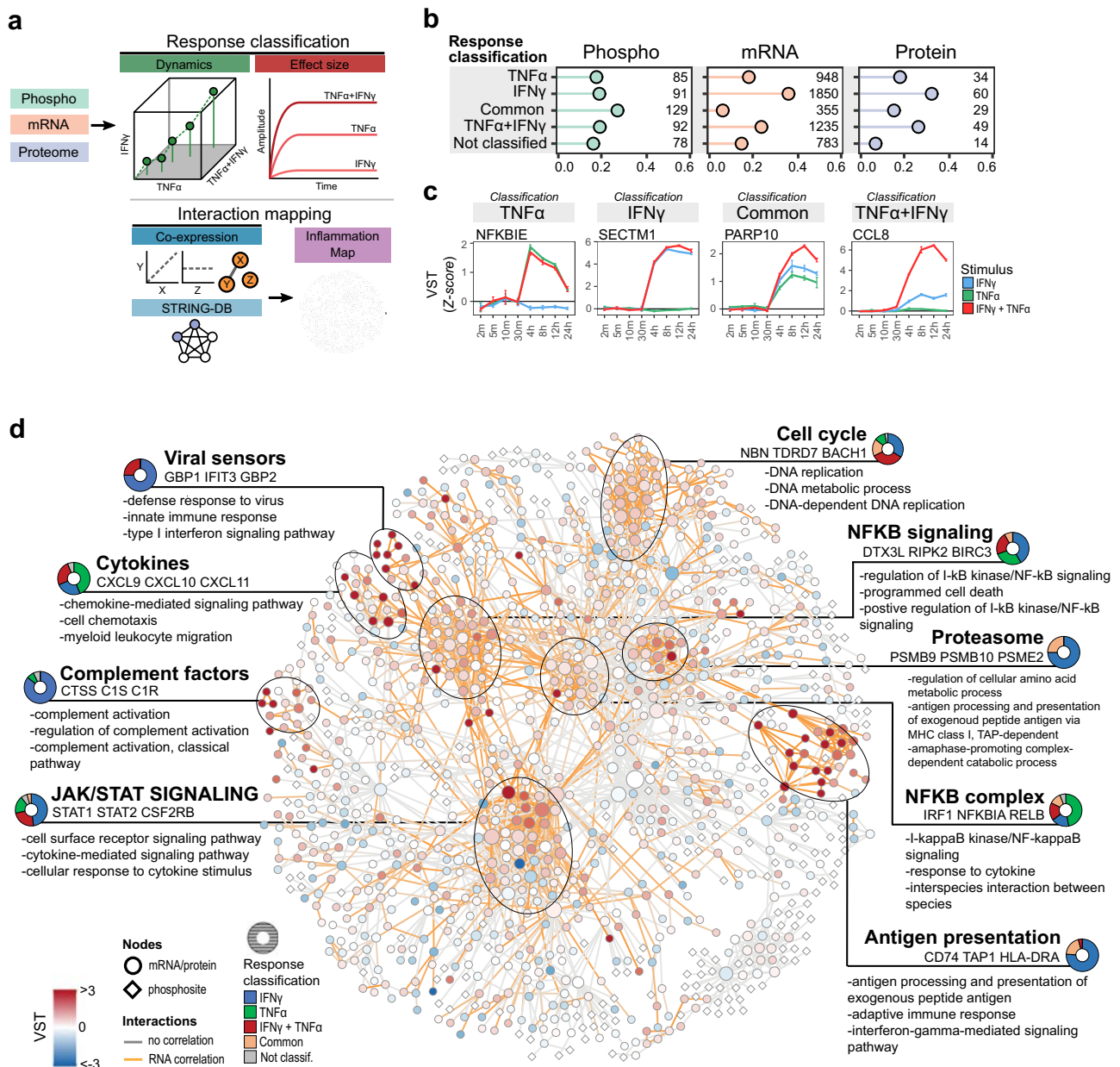


**Fig. 5** Interaction network of differentially regulated RNA/protein and phosphosites. **a** Schematic overview of generating the interaction network from significant events. **b** Bar plot showing ratio of response classification and total nodes per classification and omics levels (as indicated). **c** Line plots of normalized transcript levels (VST) of highly correlating classification transcripts. Colors indicate stimulus: TNF $\alpha$  (green), IFN $\gamma$  (blue), TNF $\alpha$  + IFN $\gamma$  (red). Circles indicate medians of replicates; error bars show standard deviation ( $n = 3$  biological replicates). **d** Interaction network of all differentially regulated mRNAs/proteins and phosphosites, filtered by high confidence interactions, nodes represent transcripts/proteins and phosphosites. Color gradient indicates median transcript levels at 24 h TNF $\alpha$  + IFN $\gamma$  stimulation ( $n = 3$  biological replicates). Per cluster are indicated: summarizing biological process, top three regulated transcripts and enriched biological processes. Donut plot indicates ratio of response classification in each cluster: TNF $\alpha$  (green), IFN $\gamma$  (blue), TNF $\alpha$  + IFN $\gamma$  (red), common (orange) and no classification (gray).

example of limited fold changes in transcripts (max. 1-fold), while protein increases over 3-fold. Complement factors were another strongly induced IFN $\gamma$  hub, especially *C1R* and *C1S* showed drastically increased upregulation of transcripts (>5-fold) (Fig. 6b). *C3*, crucial in the activation of the alternative pathway, is the only uniquely TNF $\alpha$ -induced transcript in this hub. However, whether transcript expression translated to protein increases is unclear as corresponding proteins were not detected. IFN $\gamma$  also induced a strong antigen-presenting hub (Fig. 6c). We previously reported TNF $\alpha$  induces MHCII proteins, including *HLA-A*, *HLA-B* and *HLA-C*, which we observed here too<sup>36</sup>.

However, these MHCII complex proteins as well as immunoproteasome regulator subunits (*PSME1* and *PSME2*), peptide loading proteins (*TAP1*, *TAP2*, *ERAP1* and *ERAP2*)<sup>37,38</sup> and immune checkpoint protein Programmed death- ligand 1 (*CD274*) were higher induced by IFN $\gamma$  compared to TNF $\alpha$ . Moreover, IFN $\gamma$  also induced MHCII complexes required for exogenous antigen presentation. *HLA-DR*, *HLA-DQ* and *HLA-DP* transcripts were upregulated 4–7-fold at 12–24 h of IFN $\gamma$  stimulation. Interestingly, in contrast to MHCII proteins, which were detected abundantly on the protein level, we were only able to detect *HLA-DRA*

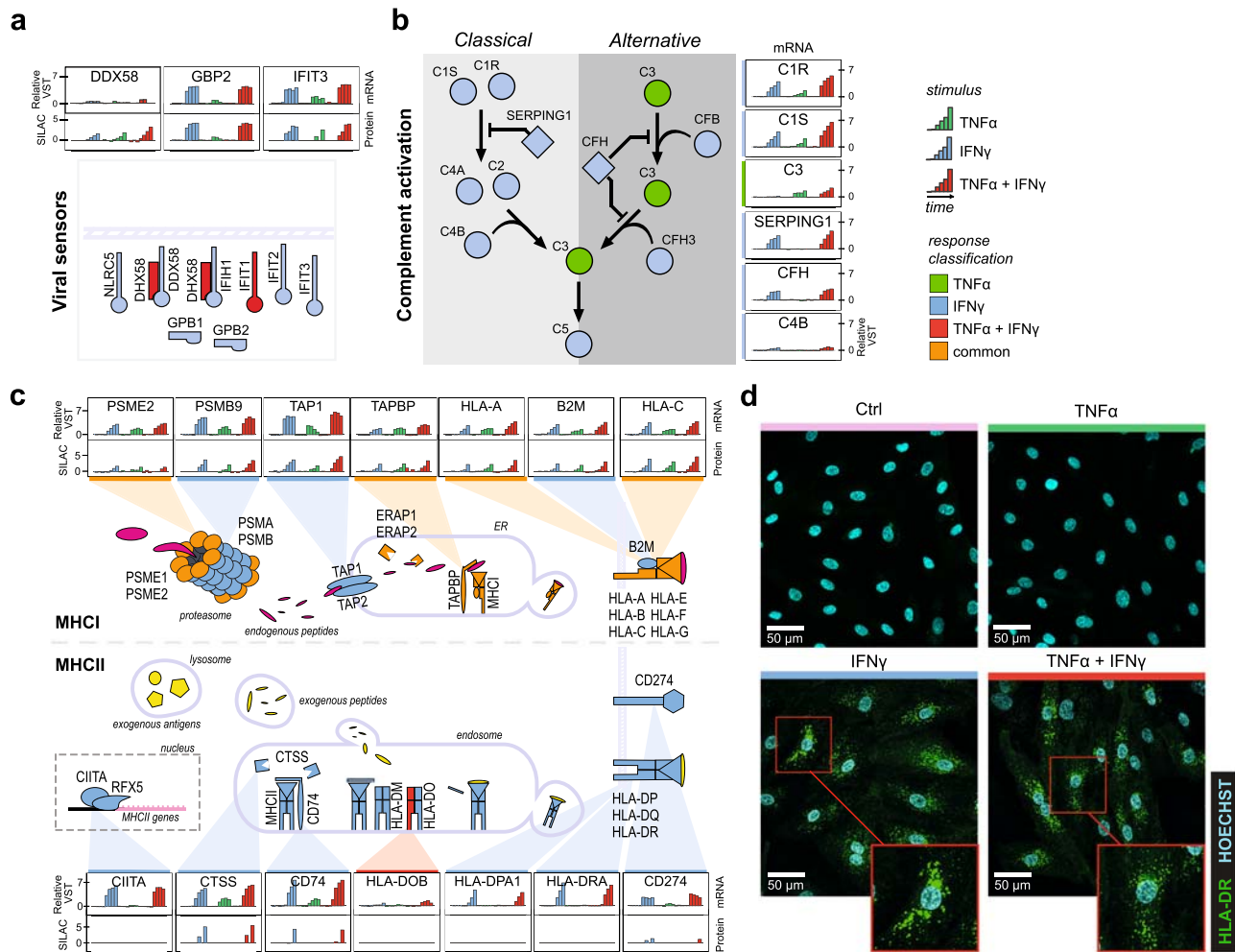


**Fig. 6** IFN $\gamma$  induces regulation of viral sensors, complement factors and antigen presentation in ECs. **a** Overview of regulated innate immune sensors in the “Viral Sensors” hub, **b** the “Complement factors” hub and **c** the “Antigen presentation” hub. Bar plots of highlighted transcripts/proteins indicate median transcript level (VST) or protein SILAC ratio per stimulus and timepoint ( $n = 3$  biological replicates). Colors indicate stimulus: TNF $\alpha$  (green), IFN $\gamma$  (blue), TNF $\alpha$  + IFN $\gamma$  (red). Node fill indicates response classification of transcript: TNF $\alpha$  (green), IFN $\gamma$  (blue), TNF $\alpha$  + IFN $\gamma$  (red), common (orange) and no classification (gray). **d** Confocal images of HLA-DR immunostaining in unstimulated ECs (Ctrl, pink) and stimulated with TNF $\alpha$ , IFN $\gamma$ , and TNF $\alpha$  + IFN $\gamma$ . HLA-DR staining is depicted in green, Hoechst staining in cyan. Representative experiment shown ( $n = 3$  biologically independent experiments). Upper limit of the display range were adjusted equally across images for visualization purposes.

and *HLA-DRB* in separate LFQ workflow experiments (Supplementary Fig. 7a). To visualize the discrepancy between MHC I and MHC II protein expression, we stained BOECs for *HLA-A/B/C* or *HLA-DR* after stimulation of TNF $\alpha$ , IFN $\gamma$  or combined stimulation. MHC I showed a clear distribution over the cell membrane, also in steady-state condition (Supplementary Fig. 7b) and in line with both transcriptome and protein data, *HLA-DR* was only observed in IFN $\gamma$  stimulated conditions. However, in contrast to the membrane distribution of *HLA-A/B/C*, *HLA-DR* was mostly localized to compartments inside the cell (Fig. 6d).

**Transcription factor networks at the basis of inflammatory states.** Next, we investigated whether regulation between the two main signaling axes, NF- $\kappa$ B and JAK/STAT, could be at the basis of the observed inflammatory states. As expected, members of the NF- $\kappa$ B complex such as *NFKB2* (P100), *NFKB1* (P40) and *RELB* were classified as “TNF $\alpha$ ”, while key mediators of the JAK/STAT pathway, *JAK1*, *JAK2*, *STAT1*, *STAT2* and *STAT3* all classified as “IFN $\gamma$ ” (Fig. 7a). Interestingly, transcripts of IFN $\gamma$  receptors *IFNGR1* and *IFNGR2* were induced by TNF $\alpha$ , while the TNF $\alpha$  receptors

*TNFR1* and *TNFR2* in the NF- $\kappa$ B signaling axis were induced by IFN $\gamma$ . Plotting the effect size of each stimulus as a ratio of the total observed combinatorial response reveals both signaling cascades showed diverse response classifications and transcripts were not exclusively regulated by one cytokine (Fig. 7b).

In a range of transcripts, the cumulative effect size of TNF $\alpha$  and IFN $\gamma$  was not equal to the total response of combined stimulation, indicating a synergistic relation. Among these were transcription factors *RELA*, *STAT5A* and *STAT6*, *JAK3*, a central kinase in IFN signal transduction<sup>39</sup>, and *LCP2*, involved in T-cell antigen receptor-mediated signaling<sup>40</sup> (Fig. 7c). We also observed synergetic downregulation of *PECAM1*, a crucial molecule in maintaining EC cell junctions<sup>41</sup>. The synergetic regulation of transcripts did not translate to the same extent into protein levels. Only at the 24 h timepoint did correlating protein abundances in the TNF $\alpha$  + IFN $\gamma$  condition exceed the cumulative abundance of both cytokine stimuli separately.

**Endothelial inflammatory states induce distinct secretomes.** Cytokine release by ECs is a direct avenue of immune modulation

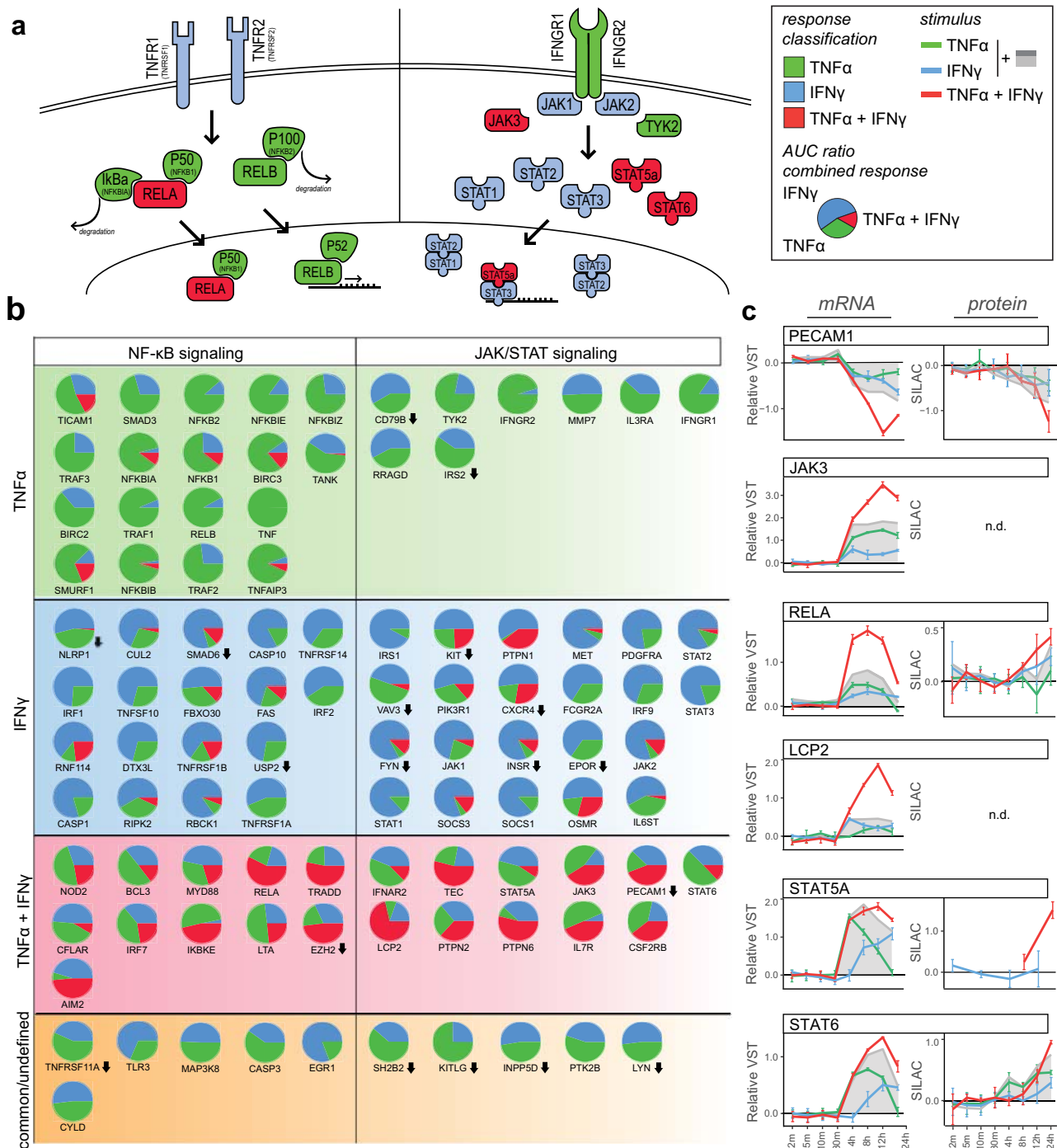


**Fig. 7** TNFα and IFNγ synergy in transcription factor signaling pathways. **a** Schematic overview of NF-κB and JAK/STAT signaling axes. Node fill color indicates response classification of transcripts: TNFα (green), IFNγ (blue), TNFα + IFNγ (red), common (orange) and no classification (gray). **b** Pie charts of transcript AUC as part of the total TNFα + IFN response: TNFα (green), IFNγ (blue), [TNFα + IFN] - TNFα - IFNγ (red). **c** Line plots of synergistic transcript levels and SILAC ratios of correlating proteins after TNFα, IFNγ and TNFα + IFNγ stimulation. The sum of separate TNFα and IFNγ regulation is shown in gray. Circles indicate medians of replicates; error bars show standard deviation (n = 3 biological replicates).

by interacting with different immune cells and both TNFα and IFNγ induced distinct cytokine transcripts and synergistic increases. However, the majority of cytokines was not detected on the protein level, potentially because of the low abundance and secretory nature of cytokines<sup>42</sup>. Therefore, we performed secretomics experiments, following the workflow as described by Deshmukh et al.<sup>43</sup>. Both secretomes and cell lysates were analyzed using high-resolution LFQ MS (Fig. 8a). Time-dependent changes were most apparent in the secretome as proteins were excreted

into the supernatant over time (Supplementary Fig. 8) and we observed limited protein changes due to stimulation at early timepoints (30 m and 4 h). However, after 24 h both TNFα and IFNγ induced 29 and 54 significant proteins, respectively, and this effect was amplified in the combined condition (177 proteins) (Fig. 8b). Generating a STRING interaction network of upregulated proteins in the combined stimulation revealed 6 protein hubs enriching for extracellular proteins, such as extracellular matrix, complement proteins and cytokines/chemokines (Fig. 8c).



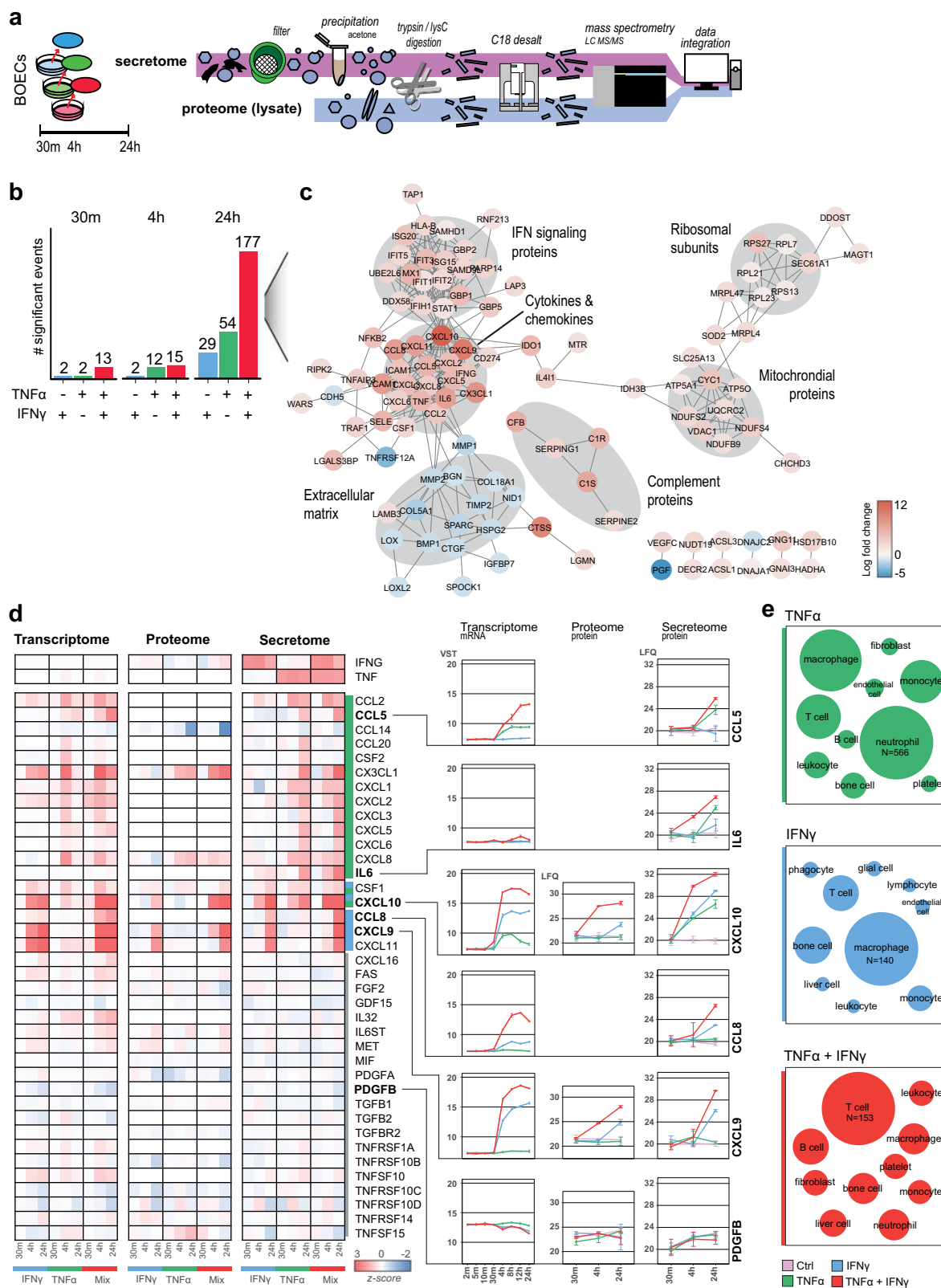


**Fig. 8 Secretome analysis of ECs after TNF $\alpha$ , IFN $\gamma$  and TNF $\alpha$  + IFN $\gamma$  stimulation. **a** Schematic overview of secretomics workflow. **b** Bar plot of number of significantly regulated proteins per stimulus (moderated *t*-test, BH-adjusted *p* < 0.01 and log<sub>2</sub> fold change > 1). Colors indicate stimulus: TNF $\alpha$  (green), IFN $\gamma$  (blue), TNF $\alpha$  + IFN $\gamma$  (red). **c** Interaction network of differentially regulated proteins after 24 h TNF $\alpha$  + IFN $\gamma$  stimulation showing protein type per hub indicated in gray. **d** Heatmap of enriched proteins in the cytokine registry per omics level showing correlating transcripts and proteins in lysate after TNF $\alpha$ , IFN $\gamma$  and TNF $\alpha$  + IFN $\gamma$  stimulation. Color gradient indicates z-scores. Several proteins are highlighted in line plots showing VST and LFG values, error bars show standard deviation (*n* = 3 biological replicates). **e** Number of papers enriching for cell type interactions by cytokines induced per stimulation. Node size represents number of papers, per stimulus largest node is set to most cited cell type (TNF $\alpha$ : *n* citations = 566, IFN $\gamma$ : *n* = 140, TNF $\alpha$  + IFN $\gamma$ : *n* = 153).**

Two hubs contained intracellular proteins namely ribosomal units and mitochondrial proteins, indicating increased cell death. Next, we used the ImmPort Cytokine Registry to create an overview of all secreted cytokines in this experiment ( $n = 44$ ) and plotted the intracellular protein abundance and transcriptome data (Fig. 8d). In line with the above-described inflammatory signatures, we observed distinct cytokines secreted per stimulus (13 for TNF $\alpha$  and 3 for IFN $\gamma$ ), cytokines excreted equally by both stimuli (*CSF1* and *CXCL10*) and 21 cytokines unaffected by a stimulus and constitutively expressed (e.g., *PDGFB*). The synergistic induction of *CCL5*, *CCL8*, *CXCL9* and *IL6* transcripts translated to increased secreted protein levels, but the fold-changes were less pronounced in the latter. Interestingly, whereas *IL6* showed minor mRNA increases it was abundantly present in the secretome. To gain an insight into the putative-affected cell types, we employed the ImmunXpresso text mining database and plotted the number of citations describing cytokine-cell interactions per released cytokine subset. For TNF $\alpha$  induced cytokines most citations described interactions with neutrophils ( $n = 566$ ), followed by macrophages and T-cells, while IFN $\gamma$ -released cytokines were cited mostly for macrophages ( $n = 140$ ), bone (marrow) cells and T-cells (Fig. 8e). Synergistically released cytokines (*CCL5*, *CCL8*, *CXCL9* and *IL6*) enriched for papers on T-cells ( $n = 153$ ), B-cells and bone (marrow) cell interactions, suggesting that each EC inflammatory state favors interactions with different immune cell types.

## Discussion

ECs are at the crossroads of inflammation and hemostasis and are increasingly recognized for their immunomodulatory role. We demonstrate TNF $\alpha$  and IFN $\gamma$  induce system-wide adaptive EC inflammatory states. Moreover, the combination of TNF $\alpha$  and IFN $\gamma$  induced a synergistic EC response. This study provides an in-depth molecular mapping on multiple regulatory levels and offers an extensive resource on the underlying regulation of endothelial inflammation.

As is well established, ECs contribute to immune cell migration directly through TNF $\alpha$  induced upregulation of *VCAM1*, *ICAM1* and *SELE*<sup>28,36,44</sup>. Here, we show that ECs, in addition to TNF $\alpha$ , can sense a plethora of cytokines and react on the proteome level, but the response remains limited for most. Moreover, we observe a large overlap between different stimuli, especially the TNF $\alpha$  cluster shared responses with both IL1- $\alpha$  and IL1- $\beta$ , in accordance with previous reports<sup>36,45</sup>. The two other overlapping clusters contained mainly chemokines which could explain the relatively limited proteomic response. Some of these, such as MIP3a (*CCL20*) and MIP5 (*CCL15*), have been implicated in trans migratory processes of monocytes and dendritic cells<sup>46,47</sup>, which could indicate these chemokines affect specific trans migratory processes instead of inducing cell-wide proteomic changes.

IFN $\gamma$  stimulation resulted in the second-highest response, which did not overlap with any of the other cytokines and highlighted the immunomodulating capacities of ECs. IFN $\gamma$  induced a strong upregulation of antiviral proteins and complement proteins. Of the latter, we observed *C1R*, *C1S* and *CFB* secretion into the extracellular matrix, showing the contribution of ECs to the regulation of the complement cascade. As expected, IFN $\gamma$  also induced a strong increase of MHCII complex proteins. ECs are implicated as modulatory antigen-presenting cells, regulating CD8+ and CD4+ T cell tolerance and transmigration and play a role in allograft rejection<sup>48–50</sup>. Interestingly, although MHCII is constitutively expressed *in vivo*, our confocal analysis revealed that after 24 h of stimulation, *HLA-DR* proteins were not expressed at the cell surface but were mostly confined to

intracellular compartments. This could be an artifact of *in vitro* culturing ablating the transport of *HLA-DR* proteins to the cell surface and potentially longer stimulation windows or a secondary trigger is necessary to facilitate cell surface expression<sup>51,52</sup>. In addition to the internal molecular mechanisms, another avenue of endothelial immunomodulation is through extracellular communication in the form of released signaling proteins. In line with intracellular processes, different proteins were secreted depending on the stimulus. TNF $\alpha$  is well studied in the context of neutrophil transmigration and cytokines released after TNF $\alpha$  stimulation did indeed enrich mostly for papers on neutrophil interactions. IFN $\gamma$  stimulation induced secretion of *CXCL9*, *CXCL10* and *CXCL11*, which all signal via the CXCR3 receptor that is mostly present on monocytes, T-cells, NK-cells, and dendritic cells<sup>53,54</sup>. However, TNF $\alpha$  does not exclusively induce granulocyte attractants (e.g., *CCL20* and *CX3CL1*) and most chemokines have chemoattractant properties for multiple leukocytes<sup>55</sup>. Combined TNF $\alpha$  and IFN $\gamma$  synergistically increased *CCL5*, *CCL8*, *CXCL9* and *IL6* levels, further nuancing which immune cells are favored by the endothelium. Moreover, *IL6* is associated with inflammatory disorders and implicated as a marker for disease severity in for example ARDS and COVID-19<sup>56,57</sup>.

Comparing the temporal nature of TNF $\alpha$  and IFN $\gamma$  responses showcased different dynamics between mRNA and proteome, while both cytokines induced a similar immediate phospho-signaling response. On the transcriptome level, TNF $\alpha$  induced a more immediate response which generally decreased within 24 h. Interestingly, TNF $\alpha$ -induced expression of surface adhesion molecules such as *VCAM1*, can last for several days, indicating a small induction can induce lasting protein expression<sup>58,59</sup>. On the contrary, IFN $\gamma$  induced mRNA expression increases steadily over time reaching peak transcript levels at 24 h, the endpoint in this study. Whether the IFN $\gamma$  response is sustained remains to be elucidated, but studies have shown a lasting proteome response for 48 h after short-term (3 h) IFN $\gamma$  stimulation windows<sup>60</sup>.

The synergetic effects of combined TNF $\alpha$  and IFN $\gamma$  stimulation in ECs have been observed in previous reports<sup>21–23</sup> and in line with these observations, combining both TNF $\alpha$  and IFN $\gamma$  resulted in system-wide cooperative regulation as well. However, protein induction was generally less pronounced compared to synergetic mRNA increases and changes in protein abundance occurred mainly between 12 and 24 h, which could indicate synergy in the proteome is more apparent at later timepoints. The molecular basis of the synergetic interplay can be multifold. One mechanism could be an increased mRNA expression by both cytokines. For example, *CXCL10* is reported to have two transcription factor binding regions, one for NF- $\kappa$ B and one for interferon sensitive response element<sup>22,61</sup> and we indeed observe combined stimulation to be a summation of both separate stimuli. Other studies have described altered mRNA half-life times through cytokine stimulation<sup>62</sup>. For example, *CCL5* mRNA can be stabilized through IFN $\gamma$  stimulation, and we indeed observe a synergetic increase in mRNA levels when combined with TNF $\alpha$  even though IFN $\gamma$  alone does not induce transcript expression<sup>63,64</sup>. In contrast, the synergetic decrease of *PECAM1* transcripts could be explained by cytokine-induced mRNA destabilization<sup>65</sup>. Moreover, these mechanisms are specifically regulated per protein. For example, *CCL5* and *CCL8*, both synergistically induced proteins, show opposite induction patterns: for *CCL5* TNF $\alpha$  induces, and IFN $\gamma$  stabilizes mRNA, while for *CCL8* these roles are reversed.

The activation of different NF- $\kappa$ B and STAT transcription factors seems to underly the different inflammatory states and we observe crosstalk in the two main activation pathways of these transcription factors. Especially synergetic induction of key mediators of these signaling axes such as NF- $\kappa$ B complex protein

*RELA* and *JAK3* and *STAT5A/6* suggests the differential activation of transcription programs through combined stimulation. Considering interactions between transcription factors such as NF- $\kappa$ B, interferon regulatory factors and STATs<sup>22,66</sup>, this drastically increases the complexity of regulation driving inflammatory states. When putting our findings in the context of *in vivo* regulation we should consider the limitations of this study. We employ BOECs as our *in vitro* model, which are less well-characterized than other used EC models such as HUVECs. However, BOECs have been shown to express mature EC markers over multiple passages, are preferred for metabolic labeling strategies due to their extensive proliferative ability and can be directly derived from adult donors and patients<sup>24,25,67–69</sup>. Variability in donor-to-donor responses is a point of concern as well<sup>70,71</sup>, but throughout this study, we employed BOECs derived from 19 different donors (Supplementary Table 2) and observed consistent inflammatory signatures throughout. Growth conditions of cultured ECs such as used matrix, 3D culturing, or flow could also affect inflammatory outcome. However, although ECs alter their cellular organization and phenotypical characteristics, proteins induced upon inflammatory triggers seem conserved between culture conditions, suggesting these additions nuance the inflammatory response instead of alternating the activated processes<sup>72,73</sup>. Ideally, an *in vitro* model combining flow and 3D culturing would be employed, but these models often lack robustness and throughput. ECs are also heterogenous between different organs and vessel-types<sup>74</sup> and it is unclear how inflammatory processes are regulated throughout ECs from different vascular beds. An important distinction considering vascular inflammatory disorders, is that between the micro- and microvasculature. Although studies have shown ECs derived from the macro- or microvasculature retain their specific differences in culture<sup>75</sup>, it is difficult to assess whether BOECs take on a macro- or micro-like vessel type as they differentiate within the *in vitro* microenvironment. Comparing steady-state mRNA data highlighted the challenges of assessing EC variation over multiple studies. We did observe overall similar relative expression levels of EC markers and TNF $\alpha$  and IFN $\gamma$  receptors, suggesting the observed cytokine responses could potentially be translated to other EC types as well<sup>30–32</sup>. To assess whether these inflammatory states are conserved between different vascular beds is a crucial step in future studies to understand tissue-specific EC inflammation. In conclusion, this study provides a detailed insight of the inflammatory states of the endothelium which is regulated through intricate transcriptional and translational control. Uncovering these molecular mechanisms is vital in understanding the paths that lead to endothelial dysfunction and its contribution to vascular inflammation.

## Methods

**Cell culture.** BOECs were isolated from healthy donors as described by Ramirez et al.<sup>24</sup>. For all experiments, except the multi-omics and secretome experiments, three different pools of three unique BOEC donors (mixed sexes and ages) were used (Supplementary Table 2). For the multi-omics and secretome experiments, BOECs from three different donors (mixed sexes and ages) were pooled. Culture flasks and dishes were coated with collagen type I (50  $\mu$ g/ml, BD biosciences) for 1 h prior to use. Cells were cultured in EC basal medium (Lonza) supplemented with 18% FCS (Bodinco) and EGM bulletkit (Lonza) unless stated otherwise. For SILAC labeling, BOECs were maintained for 5 passages as described by Beguin et al.<sup>36</sup> in custom-made EGM medium (Lonza), containing EBM2 medium (not containing Arginine and Lysine) (Lonza), EGM bulletkit (Lonza) and 18% FCS for passages 1–3 and in 18% 1 kDa dialyzed FCS for passages 4–5. Cells were SILAC labeled by the addition of isotope-labeled amino acids during all passages (light: Arg0 and Lys0, medium: Arg6 and Lys4, heavy: Arg10 and Lys8, Cambridge Isotopes). After five passage incorporation of labeled amino acids reached >95% in the total proteome.

**Stimulation.** All recombinant human cytokines used for stimulations were obtained from Peprotech (Supplementary Table 1). ECs were stimulated in three

biological replicates with 10 ng/ml per cytokine for indicated timepoints, with the exception of dose-response experiments, in which cells were stimulated at 1, 10 and 100 ng/ml. Prior to stimulation, cells were washed 3 $\times$  with PBS and stimulations were performed in endothelial basal medium (Lonza) supplemented with 18% FCS (Bodinco) and EGM bulletkit (Lonza), with the exception of SILAC BOECs and secretome experiments. SILAC BOECs were serum starved for 2 h prior to stimulation and stimulated in endothelial basal medium (Lonza) without additions. Stimulations in secretome experiments were performed in phenol-red-free endothelial basal medium (Promocell) without any additions.

**Immunofluorescence staining.** BOECs were grown to confluence on collagen-coated glass coverslips. After 4 days, cells were either not stimulated or stimulated with, TNF $\alpha$ , IFN $\gamma$  or TNF $\alpha$  + IFN $\gamma$  as described above. Cells were fixed using 4% PFA (Thermo Scientific), washed 3 $\times$  with PBS and quenched with 50 mM ammonium chloride (Sigma-Aldrich). Antibody staining steps were performed in 1% BSA (Serva), 0.1% Saponin (Sigma-Aldrich) to permeabilize cells. MHCI was stained using pan-HLA monoclonal W6/32 mouse antibody generated from hybridoma (ATCC, HB-95), HLA-DR was stained with monoclonal L243 anti-human/monkey antibody (InVivoMAB, BE0306), both at 10  $\mu$ g/ml. Alexa Fluor 488 chicken-anti-mouse conjugated secondary antibody (2  $\mu$ g/ml) was used for both stainings (Invitrogen, #A21200). Slides were fixed in Mowiol 4-88 (Polysciences). Pictures were taken on an SP8 Confocal Laser Scanning Microscope (Leica) with a 40 $\times$ /1.30 oil objective (Leica, 11506359) at 1024 $\times$ 1024 resolution. Images were processed using Fiji<sup>76</sup>. Immunostaining was performed three times in independent experiments.

**RNA sequencing.** Cells used for RNAseq analysis were lysed in RLT buffer (QIAGEN) according to the manufacturer's protocol. RNA sequencing was performed by GeneWiz (Azenta life sciences), including RNA isolation, library preparation, strand-specific RNAseq with PolyA selection and Illumina paired-end 150 bp sequencing. After quality control with FastQC, sequences were aligned to the human ChGR38.104 genome reference using STAR 2.7.8a and reads were summarized using featureCounts 2.0.1. Differential expression analysis was performed using DESeq2<sup>77</sup>, applying a significance threshold of a Benjamini-Hochberg (BH) multiple testing corrected *p* value of <0.05 and log<sub>2</sub> fold change of >1.

**Mass spectrometric analysis.** For mass spectrometry analysis of EC proteomes, cells were lysed in 1% sodium deoxycholate (Bioworld), 10 mM TCEP (Thermo Scientific), 40 mM chloroacetamide (Sigma-Aldrich), 100 mM Tris-HCl pH 8.0 (Gibco) supplemented with 1 $\times$  HALT protease/phosphatase inhibitor (Thermo Scientific). Lysates were incubated for 5 min at 95 °C and sonicated for 10 min in a sonifier bath (Branson model 2510), after which trypsin (Promega) was added in a 1:50 (w/w) protein ratio. Peptides were desalted with C18 cartridges (Agilent) according to manufacturers' instructions and where applicable phosphopeptide enrichment was performed using Fe(III)-IMAC cartridges (Agilent) as described by Post et al.<sup>78</sup> on an AssayMAP BRAVO (Agilent). For the deep proteome protein was first cleaned with HyperSep C18 Cartridges (Thermo Scientific) and HyperSep Hypercarb SPE Cartridges (Thermo Scientific). Then, samples were fractionated with the Pierce High pH reversed-phase peptide fractionation kit (Thermo Scientific) and fractions desalted with Empore C18 STAGE tips (Supelco). Fractionation was performed in triplo and obtained fractions were measured separately. For secretome analysis, samples were worked up as described in Deshmukh et al.<sup>43</sup> using minor adjustments. First, supernatants were collected and filtered using a 0.2- $\mu$ m filter (Whatman). Collected supernatants were spun down at 5000 g to remove cell debris and stored at –80 °C before further use. Samples were acetone (1:4 ratio, Biosolve) precipitated overnight at –20 °C, before precipitates were lysed with Urea (6 M, Invitrogen) + ThioUrea (2 M, Sigma-Aldrich), reduced with 10 mM DTT (40 min, Thermo Scientific), and alkylated with 55 mM IAA (Thermo Scientific) in the dark (40 min). Samples were subsequently digested with 0.5  $\mu$ g LysC/Trypsin (Thermo Scientific) overnight and desalted on Empore C18 STAGE tips (Supelco).

Peptides were separated by nanoscale C18 reverse chromatography coupled online to an Orbitrap Fusion Lumos Tribrid mass spectrometer or Orbitrap Fusion Tribrid mass spectrometer (Thermo Fisher Scientific) via a nanoelectrospray ion source at 2.15 kV. Buffer A was composed of 0.1% formic acid and buffer B of 0.1% formic acid and 80% acetonitrile. For label-free analysis, peptides were loaded for 17 min at 300 nl/min at 5% buffer B, equilibrated for 5 min at 5% buffer B (17–22 min) and eluted by increasing buffer B from 5 to 27.5% (22–122 min) and 27.5 to 40% (122–132 min), followed by a 5 min wash to 95% and a 6 min regeneration to 5%. Survey scans of peptide precursors from 375 to 1500 m/z were performed at 120,000 resolution (at 200 m/z) with a 4 $\times$ 10<sup>5</sup> ion count target. Tandem mass spectrometry was performed by isolation with the quadrupole, with isolation window 0.7, higher energy collisional dissociation (HCD) fragmentation with normalized collision energy of 30 and rapid scan mass spectrometry analysis in the ion trap. The tandem mass spectrometry (MS2) ion count target was set to 3 $\times$ 10<sup>4</sup>, and the max injection time was 20 ms. Only those precursors with charge state 2–7 were sampled for MS2. The dynamic exclusion duration was set to 30 s with a 10 ppm tolerance around the selected precursor and its isotopes.

Monoisotopic precursor selection was turned on. The instrument was run in top speed mode with 3 s cycles. All data were acquired with Xcalibur software (Thermo Fisher Scientific).

For phosphoproteomics acquisition of SILAC labeled samples, tryptic peptides were loaded for 17 min at 300 nL/min at 5% buffer B, equilibrated for 5 min at 5% buffer B (17–22 min) and eluted by increasing buffer B from 5 to 15% (22–87 min) and 15 to 38% (87–147 min), followed by a 10 min wash to 90% and a 5 min regeneration to 5%. Survey scans of peptide precursors from 350 to 1750 m/z were performed at 240 K resolution (at 200 m/z) with a  $2 \times 10^5$  ion count target. Tandem mass spectrometry was performed by isolation with the quadrupole with isolation window 1.6, HCD fragmentation with normalized collision energy of 30, and rapid scan mass spectrometry analysis in the orbitrap. The MS2 ion count target was set to  $10^5$  and the max injection time was 60 ms. Only those precursors with charge state 2–7 were sampled for MS2. The dynamic exclusion duration was set to 60 s with a 10-ppm tolerance around the selected precursor and its isotopes. Monoisotopic precursor selection was turned on. The instrument was run in top N mode. For SILAC proteome samples a slightly adjusted protocol was used: peptides were loaded for 17 min at 300 nL/min at 5% buffer B, equilibrated for 5 min at 5% buffer B (17–22 min) and eluted by increasing buffer B from 5 to 28% (22–80 min) and 28 to 40% (80–85 min), followed by a 5 min wash to 95% and a 5 min regeneration to 5%. Survey scan was set to 240 K with a  $1 \times 10^6$  ion count target. Tandem mass spectrometry was performed on the 10 most intense ions by isolation using the quadrupole and analysis in the ion trap at a resolution of 30 K. The MS2 ion count target was set to  $5 \times 10^4$  with a maximum injection time of 60 ms. The instrument was run in top speed mode with 3 s cycles. All data were acquired with Xcalibur software.

**Mass spectrometry data analysis.** The RAW mass spectrometry files were processed with the MaxQuant computational platform, 1.6.2.10. Proteins and peptides were identified using the Andromeda search engine by querying the human Uniprot database (release 2019). Standard settings with the additional options match between runs, LFQ, IBAQ, and unique peptides for quantification were selected. For SILAC samples, multiplicity was set to 3 (for Arg0 and Lys0, Arg6 and Lys4 and Arg10 and Lys8) and the re-quantify option was enabled, where applicable Phospho STY was set as a dynamic modification. Data were analyzed using R 3.5.2/RStudio 1.1.456. For label-free data, “reverse”, “potential contaminants” and “only identified by site” peptides were filtered out. Proteins and phosphosites were filtered for at least 100% valid values per experimental group. LFQ values were transformed in  $\log_2$  scale. Missing values were imputed by a normal distribution (width = 0.3, shift = 1.8), assuming these proteins were close to the detection limit. Batch effects were corrected for using ComBat in the sva package. Label-free statistical analyses were performed using LIMMA<sup>79</sup>. For SILAC data analysis, statistical analysis was performed using a linear model without intercepting non-imputed data. For clustering purposes, missing values were imputed by linear approximation using the Amelia package. For both label-free and SILAC data, moderated *t*-tests were used to determine differentially abundant proteins<sup>80</sup>. A BH-adjusted  $p < 0.05$  and  $\log_2$  fold change  $> 1$  was considered significant and relevant. For label-free secretomics data, a BH-adjusted  $p < 0.01$  and  $\log_2$  fold change  $> 1$  was used as the significance threshold.

**Mapping cytokine-endothelial interactions.** Receptor and ligand definition was performed as described by Rieckmann et al.<sup>8</sup>. In brief, “extracellular” keywords or “GPI-anchor” topology domain based on the Uniprot knowledge base annotations were used to define receptor proteins. STRING-DB interactions with known interacting proteins (combined scores  $> 0.4$ ) were selected and annotated for Uniprot “secreted” and “signal” keywords or GO:CC “extracellular space” and “extracellular region” terms to define receptor ligands. Connections between receptors and ligands were visualized in Cytoscape 3.8.0.

**Response classification and inflammation map construction.** RNA, protein and phosphosite responses in the TNF $\alpha$  + IFN $\gamma$  stimulation were classified based on a combined assessment of Pearson correlation with single TNF $\alpha$  and IFN $\gamma$  conditions and effect size by determining areas under the curves using the flux packages. First dynamics were categorized as either S1-TNF $\alpha$  shape (correlation coefficient  $> 0.7$  with TNF $\alpha$  and  $< 0.7$  with IFN $\gamma$  stimulation); S2-IFN $\gamma$  shape (correlation coefficient  $< 0.7$  with TNF $\alpha$  and  $> 0.7$  with IFN $\gamma$  stimulation); S3-common shape (correlation coefficient  $> 0.7$  with TNF $\alpha$  and  $> 0.7$  with IFN $\gamma$  stimulation) or S4-TNF $\alpha$  + IFN $\gamma$  shape (correlation coefficient  $< 0.3$  with TNF $\alpha$  and  $< 0.3$  with IFN $\gamma$  stimulation). Effect sizes were categorized as E1-TNF $\alpha$  effect (AUC ratios TNF $\alpha$  + IFN $\gamma$  stimulation/TNF $\alpha$  stimulation  $< 2$  and TNF $\alpha$  + IFN $\gamma$  stimulation/IFN $\gamma$  stimulation  $> 2$ ); E2-IFN $\gamma$  effect (AUC ratios TNF $\alpha$  + IFN $\gamma$  stimulation/TNF $\alpha$  stimulation  $> 2$  and TNF $\alpha$  + IFN $\gamma$  stimulation/IFN $\gamma$  stimulation  $< 2$ ), and E3-TNF $\alpha$  + IFN $\gamma$  effect (AUC ratios TNF $\alpha$  + IFN $\gamma$  stimulation/TNF $\alpha$  stimulation  $> 2$  and TNF $\alpha$  + IFN $\gamma$  stimulation/IFN $\gamma$  stimulation  $> 2$ ). Classifications were set to common if S3 but not E3 criteria were fulfilled; TNF $\alpha$  classification: S1 or S3 + E1; IFN $\gamma$  classification: S2 or S3 + E2; TNF $\alpha$  + IFN $\gamma$  classification: S3 or E3 classifications were fulfilled. If not fulfilling any shape or effect size cutoffs, classification was set to “not classified”.

To construct an inflammation map, all transcript, proteins and phosphosites that were statically significant in the TNF $\alpha$  + IFN $\gamma$  stimulation were selected and

collapsed to gene names. Based on STRING-DB interaction scores  $> 0.9$  gene names were connected with edges. Edges between phosphosites, corresponding proteins and transcript were manually appended to the network. This network was visualized in Cytoscape 3.8.0. We first obtained the “EdgeBetweenness” using the “Analyse Network” function, after which we used “Edge-weighted Spring Embedded Layout” to visualize the network. We highlighted interaction hubs based on closeness of nodes, overall regulation levels and biological overlap.

**Co-expression, term enrichment and EC comparative analyses.** Co-expression analysis was performed using the WGCNA package<sup>81</sup> using a signed network and a soft power of 4, minClusterSize was set to 10. GO term enrichment and pathway analyses were performed using clusterPofiler<sup>27</sup> and rWikiPathways<sup>82</sup> packages, enrichments with a BH-adjusted  $p$  value  $< 0.05$  were considered significant. For the comparative EC analyses, we selected three studies with various primary cultured ECs. To compare datasets, batch effects were removed and normalized using the Limma package<sup>79</sup>.

**Statistics and reproducibility.** Statistical tests are employed and significance cut-off values are indicated per experiment in the methods section. For reproducibility, ECs from 19 different donors were randomly combined in different pools of three donors (Supplementary Table 2). All stimulations were performed in at least three biological replicates, as indicated in per experiment.

**Reporting summary.** Further information on research design is available in the Nature Portfolio Reporting Summary linked to this article.

## Data availability

The mass spectrometry proteomics data have been deposited to the ProteomeXchange Consortium via the PRIDE<sup>83</sup> partner repository with the dataset identifier PXD036582. The mRNA sequencing data have been deposited in NCBI’s Gene Expression Omnibus<sup>84</sup> and are accessible through GE Series accession number (GSE121311). Source data used for all figures in this study can be found in Supplementary Data 1–5. Any remaining information can be obtained from the corresponding author upon reasonable request.

## Code availability

In-house written scripts are available from the corresponding author upon reasonable request.

Received: 16 December 2022; Accepted: 2 May 2023;

Published online: 15 May 2023

## References

- Galley, H. F. & Webster, N. R. Physiology of the endothelium. *Br. J. Anaesth.* **93**, 105–113 (2004).
- Kaufmann, J. E. et al. Vasopressin-induced von Willebrand factor secretion from endothelial cells involves V2 receptors and cAMP. *J. Clin. Invest.* **106**, 107–116 (2000).
- Ashina, K. et al. Histamine induces vascular hyperpermeability by increasing blood flow and endothelial barrier disruption in vivo. *PLoS One* **10**, e0132367 (2015).
- Rabiet, M.-J. et al. Thrombin-induced increase in endothelial permeability is associated with changes in cell-to-cell junction organization. *Arterioscler. Thromb. Vasc. Biol.* **16**, 488–496 (1996).
- Pober, J. S. & Sessa, W. C. Evolving functions of endothelial cells in inflammation. *Nat. Rev. Immunol.* **7**, 803–815 (2007).
- Amersfoort, J., Eelen, G. & Carmeliet, P. Immunomodulation by endothelial cells—partnering up with the immune system. *Nat. Rev. Immunol.* **22**, 576–588 (2022).
- Shilts, J. et al. A physical wiring diagram for the human immune system. *Nature* **608**, 397–404 (2022).
- Rieckmann, J. C. et al. Social network architecture of human immune cells unveiled by quantitative proteomics. *Nat. Immunol.* **18**, 583–593 (2017).
- Dominguez Conde, C. et al. Cross-tissue immune cell analysis reveals tissue-specific features in humans. *Science* **376**, eabl5197 (2022).
- Bux, J. & Sachs, U. J. H. The pathogenesis of transfusion-related acute lung injury (TRALI). *Br. J. Haematol.* **136**, 788–799 (2007).
- Sillman, C. C. The two-event model of transfusion-related acute lung injury. *Crit. Care Med.* **34**, S124–S131 (2006).
- Middleton, J. et al. Endothelial cell phenotypes in the rheumatoid synovium: activated, angiogenic, apoptotic and leaky. *Arthritis Res. Ther.* **6**, 60–72 (2004).

13. Aird, W. C. The role of the endothelium in severe sepsis and multiple organ dysfunction syndrome. *Blood* **101**, 3765–3777 (2003).
14. Millar, F. R., Summers, C., Griffiths, M. J., Toshner, M. R. & Proudfoot, A. G. The pulmonary endothelium in acute respiratory distress syndrome: insights and therapeutic opportunities. *Thorax* **71**, 462–473 (2016).
15. Teuwen, L. A., Geldhof, V., Pasut, A. & Carmeliet, P. COVID-19: the vasculature unleashed. *Nat. Rev. Immunol.* **20**, 389–391 (2020).
16. Bermejo-Martin, J. F., Almansa, R., Torres, A., Gonzalez-Rivera, M. & Kelvin, D. J. COVID-19 as a cardiovascular disease: the potential role of chronic endothelial dysfunction. *Cardiovasc. Res.* **116**, E132–E133 (2020).
17. Ghiță, A. C., Ilie, L. & Ghiță, A. M. The effects of inflammation and anti-inflammatory treatment on corneal endothelium in acute anterior uveitis. *Rom. J. Ophthalmol.* **63**, 161–165 (2019).
18. Ni, M., Chan, C. C., Nussenblatt, R. B., Li, S. Z. & Mao, W. Iris inflammatory cells, fibronectin, fibrinogen, and immunoglobulin in various ocular diseases. *Arch. Ophthalmol.* **106**, 392–395 (1988).
19. Diaz-Ricart, M. et al. Endothelial damage, inflammation and immunity in chronic kidney disease. *Toxins (Basel)*. **12**, 361 (2020).
20. Karki, R. et al. Synergism of TNF- $\alpha$  and IFN- $\gamma$  triggers inflammatory cell death, tissue damage, and mortality in SARS-CoV-2 infection and cytokine shock syndromes. *Cell* **184**, 149–168.e17 (2021).
21. Mehta, N. N. et al. IFN- $\gamma$  and TNF- $\alpha$  synergism may provide a link between psoriasis and inflammatory atherogenesis. *Sci. Rep.* **7**, 13831 (2017).
22. Clarke, D. L. et al. TNF $\alpha$  and IFN $\gamma$  synergistically enhance transcriptional activation of CXCL10 in human airway smooth muscle cells via STAT-1, NF- $\kappa$ B, and the transcriptional coactivator CREB-binding protein. *J. Biol. Chem.* **285**, 29101–29110 (2010).
23. Johnson, D. R. & Pober, J. S. HLA class I heavy-chain gene promoter elements mediating synergy between tumor necrosis factor and interferons. *Mol. Cell. Biol.* **14**, 1322–1332 (1994).
24. Martin-Ramirez, J., Hofman, M., van den Biggelaar, M., Hebbel, R. P. & Voorberg, J. Establishment of outgrowth endothelial cells from peripheral blood. *Nat. Protoc.* **7**, 1709–1715 (2012).
25. Ingram, D. A. et al. Identification of a novel hierarchy of endothelial progenitor cells using human peripheral and umbilical cord blood. *Blood* **104**, 2752–2760 (2004).
26. Kveler, K. et al. Immune-centric network of cytokines and cells in disease context identified by computational mining of PubMed. *Nat. Biotechnol.* **36**, 651–659 (2018).
27. Yu, G., Wang, L. G., Han, Y. & He, Q. Y. ClusterProfiler: an R package for comparing biological themes among gene clusters. *OMICS* **16**, 284–287 (2012).
28. Pober, J. S. & Cotran, R. S. Cytokines and endothelial cell biology. *Physiol. Rev.* **70**, 427–451. <https://doi.org/10.1152/physrev.1990.70.2.427> (1990).
29. Khan, S. et al. EndoDB: a database of endothelial cell transcriptomics data. *Nucleic Acids Res.* **47**, D736–D744 (2019).
30. Aranguren, X. L. et al. Unraveling a novel transcription factor code determining the human arterial-specific endothelial cell signature. *Blood* **122**, 3982–3992 (2013).
31. Long, L. et al. Selective enhancement of endothelial BMPR-II with BMP9 reverses pulmonary arterial hypertension. *Nat. Med.* **21**, 777–785 (2015).
32. Rombouts, C. et al. Transcriptomic profiling suggests a role for IGFBP5 in premature senescence of endothelial cells after chronic low dose rate irradiation. *Int. J. Radiat. Biol.* **90**, 560–574 (2014).
33. Agirre, X. et al. Unraveling a novel transcription factor code inductive for the human arterial-specific endothelial cell signature. *Biostudies E-GEOD-43475*. <https://www.ebi.ac.uk/biostudies/arrayexpress/studies/E-GEOD-43475> (2014).
34. Quintens, R. & Aerts, A. Microarray analysis of human umbilical vein endothelial cells (HUVECs) chronically irradiated with low dose-rate of ionizing radiation for one, three and six weeks. *Biostudies E-MTAB-6521*. <https://www.ebi.ac.uk/biostudies/arrayexpress/studies/E-MTAB-6521> (2018).
35. Gräf, S. & Morrell, N. W. BMP9\_BMPR2\_PAEC\_BOEC. *Biostudies E-MTAB-2495*. <https://www.ebi.ac.uk/biostudies/arrayexpress/studies/E-MTAB-2495> (2015).
36. Béguin, E. P. et al. Integrated proteomic analysis of tumor necrosis factor  $\alpha$  and interleukin 1 $\beta$ -induced endothelial inflammation. *J. Proteom.* **192**, 89–101 (2019).
37. McCarthy, M. K. & Weinberg, J. B. The immunoproteasome and viral infection: a complex regulator of inflammation. *Front. Microbiol.* **6**, 21 (2015).
38. van den Eshof, B. L., Medfai, L., Nolfi, E., Wawrzyniuk, M. & Sijts, A. J. A. M. The function of immunoproteasomes—an immunologists’ perspective. *Cells* **10**, 3360 (2021).
39. Morris, R., Kershaw, N. J. & Babon, J. J. The molecular details of cytokine signaling via the JAK/STAT pathway. *Protein Sci.* **27**, 1984–2009 (2018).
40. Navas, V. H., Cucho, C., Alcover, A. & Di Bartolo, V. Serine phosphorylation of SLP76 is dispensable for T cell development but modulates helper T cell function. *PLoS One* **12**, e0170396 (2017).
41. Lertkiatmongkol, P., Liao, D., Mei, H., Hu, Y. & Newman, P. J. Endothelial functions of platelet/endothelial cell adhesion molecule-1 (CD31). *Curr. Opin. Hematol.* **23**, 253–259 (2016).
42. Skalnikova, H. K., Cizkova, J., Cervenka, J. & Vodicka, P. Advances in proteomic techniques for cytokine analysis: focus on melanoma research. *Int. J. Mol. Sci.* **18**, 2697 (2017).
43. Deshmukh, A. S. et al. Proteomics-based comparative mapping of the secretomes of human brown and white adipocytes reveals EPDR1 as a novel batokine. *Cell Metab.* **30**, 963–975.e7 (2019).
44. Springer, T. A. Traffic signals for lymphocyte recirculation and leukocyte emigration: the multistep paradigm review. *Cell* **76**, 301–314 (1994).
45. Pober, J. S. Warner-Lambert/Parke-Davis award lecture. Cytokine-mediated activation of vascular endothelium. Physiology and pathology. *Am. J. Pathol.* **133**, 426–433 (1988).
46. D’Amico, G. et al. Adhesion, transendothelial migration, and reverse transmigration of in vitro cultured dendritic cells. *Blood* **92**, 207–214 (1998).
47. Meissner, A. et al. CC chemokine ligand 20 partially controls adhesion of naive B cells to activated endothelial cells under shear stress. *Blood* **102**, 2724–2727 (2003).
48. Al-Lamki, R. S., Bradley, J. R. & Pober, J. S. Endothelial cells in allograft rejection. *Transplantation* **86**, 1340–134 (2008).
49. Manes, T. D. & Pober, J. S. Antigen presentation by human microvascular endothelial cells triggers ICAM-1-dependent transendothelial protrusion by, and fractalkine-dependent transendothelial migration of, effector memory CD4 + T cells. *J. Immunol.* **180**, 8386–8392 (2008).
50. von Oppen, N. et al. Systemic antigen cross-presented by liver sinusoidal endothelial cells induces liver-specific CD8 T-cell retention and tolerization. *Hepatology* **49**, 1664–1672 (2009).
51. Wijdeven, R. H. et al. Chemical and genetic control of IFN $\gamma$ -induced MHCII expression. *EMBO Rep.* **19**, e45553 (2018).
52. Pober, J. S., Merola, J., Liu, R. & Manes, T. D. Antigen presentation by vascular cells. *Front. Immunol.* **8**, 1907 (2017).
53. Groom, J. R. & Luster, A. D. CXCR3 ligands: redundant, collaborative and antagonistic functions. *Immunol. Cell Biol.* **89**, 207–215 (2011).
54. Tokunaga, R. et al. CXCL9, CXCL10, CXCL11/CXCR3 axis for immune activation – a target for novel cancer therapy. *Cancer Treat. Rev.* **63**, 40–47 (2018).
55. Hughes, C. E. & Nibbs, R. J. B. A guide to chemokines and their receptors. *FEBS J.* **285**, 2944–2971 (2018).
56. Aisiku, I. P. et al. Plasma cytokines IL-6, IL-8, and IL-10 are associated with the development of acute respiratory distress syndrome in patients with severe traumatic brain injury. *Crit. Care* **20**, 288 (2016).
57. Shekhawat, J. et al. Interleukin-6 perpetrator of the COVID-19 cytokine storm. *Indian J. Clin. Biochem.* **36**, 440–450 (2021).
58. Croft, D., McIntyre, P., Wibulswas, A. & Kramer, I. Sustained elevated levels of VCAM-1 in cultured fibroblast-like synoviocytes can be achieved by TNF- $\alpha$  in combination with either IL-4 or IL-13 through increased mRNA stability. *Am. J. Pathol.* **154**, 1149–1158 (1999).
59. Chu, L.-Y., Hsueh, Y.-C., Cheng, H.-L. & Wu, K. K. Cytokine-induced autophagy promotes long-term VCAM-1 but not ICAM-1 expression by degrading late-phase I $\kappa$ B $\alpha$ . *Sci. Rep.* **7**, 12472 (2017).
60. Valenzuela, N. M. IFN $\gamma$ , and to a lesser extent TNF $\alpha$ , provokes a sustained endothelial costimulatory phenotype. *Front. Immunol.* **12**, 648946 (2021).
61. Majumder, S. et al. p48/STAT-1-containing complexes play a predominant role in induction of IFN-inducible protein 10 kDa (IP-10) by IFN- $\gamma$  alone or in synergy with TNF- $\alpha$ . *J. Immunol.* **161**, 4736–4744. <http://www.jimmunol.org/> (1998).
62. Hamilton, T. A. et al. Chemokine and chemoattractant receptor expression: post-transcriptional regulation. *J. Leukoc. Biol.* **82**, 213–219 (2007).
63. Lee, A. H., Hong, J. H. & Seo, Y. S. Tumor necrosis factor- $\alpha$  and interferon- $\gamma$  synergistically activate the RANTES promoter through nuclear factor kappaB and interferon regulatory factor 1 (IRF-1) transcription factors. *Biochem. J.* **350 Pt 1**, 131–138 (2000).
64. Homma, T. et al. Cooperative activation of CCL5 expression by TLR3 and tumor necrosis factor- $\alpha$  or interferon- $\gamma$  through nuclear factor- $\kappa$ B or STAT-1 in airway epithelial cells. *Int. Arch. Allergy Immunol.* **152**, 9–17 (2010).
65. Stewart, R. J., Kashour, T. S. & Marsden, P. A. Vascular endothelial platelet endothelial adhesion molecule-1 (PECAM-1) expression is decreased by TNF- $\alpha$  and IFN- $\gamma$ . Evidence for cytokine-induced destabilization of messenger ribonucleic acid transcripts in bovine endothelial cells. *J. Immunol.* **156**, 1221–1228 (1996).
66. Czerkies, M. et al. Cell fate in antiviral response arises in the crosstalk of IRF, NF- $\kappa$ B and JAK/STAT pathways. *Nat. Commun.* **9**, 493 (2018).
67. Mathur, T., Tronolone, J. J. & Jain, A. Comparative analysis of blood-derived endothelial cells for designing next-generation personalized organ-on-chips. *J. Am. Heart Assoc.* **10**, e022795 (2021).
68. Yuan, Y., Altalhi, W. A., Ng, J. J. & Courtman, D. W. Derivation of human peripheral blood derived endothelial progenitor cells and the role of osteopontin surface modification and eNOS transfection. *Biomaterials* **34**, 7292–7301 (2013).
69. Toshner, M. et al. Transcript analysis reveals a specific HOX signature associated with positional identity of human endothelial cells. *PLoS One* **9**, e91334 (2014).

70. Bender, J. R., Sadeghi, M. M., Watson, C., Pfau, S. & Pardi, R. Heterogeneous activation thresholds to cytokines in genetically distinct endothelial cells: evidence for diverse transcriptional responses. *Proc. Natl Acad. Sci. USA*. **91**, 3994–3998 (1994).
71. Filonov, D. et al. Initial assessment of variability of responses to toxicants in donor-specific endothelial colony forming cells. *Front. Public Health* **6**, 369 (2018).
72. Wilcox, E. C. & Edelman, E. R. Substratum interactions determine immune response to allogeneic transplants of endothelial cells. *Front. Immunol.* **13**, 946794 (2022).
73. Béguin, E. P. et al. Flow-induced reorganization of laminin-integrin networks within the endothelial basement membrane uncovered by proteomics. *Mol. Cell. Proteom.* **19**, 1179–1192 (2020).
74. Kalucka, J. et al. Single-cell transcriptome atlas of murine endothelial cells. *Cell* **180**, 764–779.e20 (2020).
75. Stolz, D. B. & Jacobson, B. S. Macro- and microvascular endothelial cells in vitro: maintenance of biochemical heterogeneity despite loss of ultrastructural characteristics. *Vitr. Cell. Dev. Biol.* **27A**, 169–182 (1991).
76. Schindelin, J. et al. Fiji: an open-source platform for biological-image analysis. *Nat. Methods* **9**, 676–682 (2012).
77. Love, M. I., Huber, W. & Anders, S. Moderated estimation of fold change and dispersion for RNA-seq data with DESeq2. *Genome Biol.* **15**, 550 (2014).
78. Post, H. et al. Robust, sensitive, and automated phosphopeptide enrichment optimized for low sample amounts applied to primary hippocampal neurons. *J. Proteome Res.* **16**, 728–737 (2017).
79. Ritchie, M. E. et al. Limma powers differential expression analyses for RNA-sequencing and microarray studies. *Nucleic Acids Res.* **43**, e47 (2015).
80. Phipson, B., Lee, S., Majewski, I. J., Alexander, W. S. & Smyth, G. K. Robust hyperparameter estimation protects against hypervariable genes and improves power to detect differential expression. *Ann. Appl. Stat.* **10**, 946–963 (2016).
81. Langfelder, P. & Horvath, S. WGCNA: an R package for weighted correlation network analysis. *BMC Bioinforma.* **9**, 559 (2008).
82. Slenter, D. N. et al. WikiPathways: a multifaceted pathway database bridging metabolomics to other omics research. *Nucleic Acids Res.* **46**, D661–D667 (2018).
83. Perez-Riverol, Y. et al. The PRIDE database resources in 2022: a hub for mass spectrometry-based proteomics evidences. *Nucleic Acids Res.* **50**, D543–D552 (2022).
84. Edgar, R., Domrachev, M. & Lash, A. E. Gene Expression Omnibus: NCBI gene expression and hybridization array data repository. *Nucleic Acids Res.* **30**, 207–210 (2002).

## Acknowledgements

This work was supported by the Landsteiner Foundation for Blood Transfusion Research grants LSBR-1517 awarded to M.v.d.B. and LSBR-1923 awarded to A.J.H. and M.v.d.B.

## Author contributions

S.A.G. performed experiments, analyzed data, and drafted the manuscript. E.R.S. analyzed data. E.F.J.J. and B.L.v.d.E. performed experiments. F.P.J.v.A. and C.v.d.Z. performed mass-spec data acquisition. A.B.M supervised research. A.J.H. designed the study, performed experiments, supervised research, analyzed data, and drafted the manuscript. M.v.d.B. designed the study, supervised research, and drafted the manuscript. All authors read and approved the final version of the manuscript.

## Competing interests

The authors declare no competing interests.

## Additional information

**Supplementary information** The online version contains supplementary material available at <https://doi.org/10.1038/s42003-023-04897-w>.

**Correspondence** and requests for materials should be addressed to Maartje van den Biggelaar.

**Peer review information** *Communications Biology* thanks Thomas Mohr and the other, anonymous, reviewer(s) for their contribution to the peer review of this work. Primary Handling Editors: Zhijuan Qiu and Anam Akhtar. A peer review file is available.

**Reprints and permission information** is available at <http://www.nature.com/reprints>

**Publisher's note** Springer Nature remains neutral with regard to jurisdictional claims in published maps and institutional affiliations.



**Open Access** This article is licensed under a Creative Commons Attribution 4.0 International License, which permits use, sharing, adaptation, distribution and reproduction in any medium or format, as long as you give appropriate credit to the original author(s) and the source, provide a link to the Creative Commons license, and indicate if changes were made. The images or other third party material in this article are included in the article's Creative Commons license, unless indicated otherwise in a credit line to the material. If material is not included in the article's Creative Commons license and your intended use is not permitted by statutory regulation or exceeds the permitted use, you will need to obtain permission directly from the copyright holder. To view a copy of this license, visit <http://creativecommons.org/licenses/by/4.0/>.

© The Author(s) 2023, corrected publication 2023